Journal of Geophysical Research: Earth Surface

RESEARCH ARTICLE
10.1029/2017JF004561

Key Points:
- We use radar reflectivity to estimate the basal thermal regimes of Petermann Glacier
- The onset of Petermann Glacier is composed of alternating bands of frozen and thawed bed
- Basal thermal regime and basal meltwater production control the behavior and stability of Petermann Glacier

Supporting Information:
- Supporting Information S1
- Data Set S1
- Data Set S2

Correspondence to:
W. Chu,
wchu28@stanford.edu

Citation:
Chu, W., Schroeder, D. M., Seroussi, H., Creyts, T. T., & Bell, R. E. (2018). Complex basal thermal transition near the onset of Petermann Glacier, Greenland. *Journal of Geophysical Research: Earth Surface, 123*. https://doi.org/10.1029/2017JF004561

Received 15 NOV 2017
Accepted 10 APR 2018
Accepted article online 25 APR 2018

Complex Basal Thermal Transition Near the Onset of Petermann Glacier, Greenland

W. Chu[1], D. M. Schroeder[1,2], H. Seroussi[3], T. T. Creyts[4], and R. E. Bell[4]

[1]Department of Geophysics, School of Earth, Energy and Environmental Sciences, Stanford University, Stanford, CA, USA, [2]Department of Electrical Engineering, School of Engineering, Stanford University, Stanford, CA, USA, [3]Jet Propulsion Laboratory, California Institute of Technology, Pasadena, CA, USA, [4]Division of Marine Geology and Geophysics Division, Lamont-Doherty Earth Observatory of Columbia University, Palisades, NY, USA

Abstract The basal thermal regime of ice sheets exerts a strong control on ice-sheet stability and the onset of rapidly streaming flow. However, the nature of this thermal transition where sliding initiates is largely unconstrained by geophysical observations. In the Greenland Ice Sheet, topographic troughs or elevated geothermal heat fluxes typically define the onset of outlet glaciers. In contrast, Petermann Glacier in Northern Greenland does not have any distinct bed troughs or localized geothermal heating associated with its onset, making it an ideal site to investigate the basal thermal state and examine its role in the onset of Petermann Glacier. Here we use radar bed reflectivity and an ice-sheet thermomechanical model to examine the basal thermal regime beneath Petermann Glacier. Our results reveal a complex thermal transition near the onset of Petermann Glacier. As the bed shifts from largely frozen to largely thawed with increasing distances from the ice divide, our results show that this thermal transition happens through alternating bands of frozen and thawed bands. The complex thermal state across the onset region suggests that lateral meltwater injection and local meltwater production determine the location of Petermann Glacier. Given the lack of topographic pinning at the onset location, the upstream margin of Petermann is vulnerable to migrate depending on a combination of advective cooling and meltwater supply from the interior of the ice sheet.

Plain Language Summary Petermann Glacier is one of the largest outlet glaciers in Northern Greenland. Its fast-flowing ice reaches deep into the ice interior, drawing ~13 km^3 of ice every year from the divide to the coast. But what determines the onset of this enigmatic glacier? Different from other large outlet glaciers in Greenland, the head of Petermann Glacier does not sit in any distinct subglacial basins. Without this topographic forcing to promote its ice velocity, other internal process related to the temperature of ice sheet base could be the critical factor that controls the location of Petermann Glacier. However, currently, there are very few observations on this basal thermal condition. Using a novel ice-penetrating radar analysis technique, we present the first detailed observations on the basal thermal condition of Petermann Glacier. Our results reveal that as the ice sheet bed begins to warm up as the ice moves closer to the coast, the bed shifts from a frozen to a thawed condition multiple times before it reaches a persistent thawed condition. These results explain why ice sheet models that assume a simple, single frozen-to-thawed bed transition struggle to reproduce the upstream margin of Petermann Glacier accurately.

1. Introduction

A thawed or frozen thermal state at the base of the ice sheet can increase or reduce the friction of the ice sheet at its bed. The thermal state impacts the amount of water in the subglacial hydrologic system that influences the rate of basal sliding and ice velocity. Beneath the Greenland Ice Sheet, the basal thermal state changes from a frozen to thawed bed with increasing distance from the ice divides towards the ice sheet margin. Constraining the location and character of this thermal transition is crucial to the understanding of how basal friction evolves as well as the relative roles of water and basal temperature in initiating fast flow.

Recent studies of radar stratigraphy and ice sheet models have characterized the large-scale configuration of basal thermal states across Greenland (Aschwanden et al., 2012; Greve, 1997; MacGregor et al., 2016; Rogozhina et al., 2016; Seroussi et al., 2013). These studies agree that the bed beneath the northeast and southwest regions is largely thawed and the bed beneath the central ice divides is frozen. Elsewhere, however, there is a poor agreement between these observations and models (MacGregor et al., 2016).

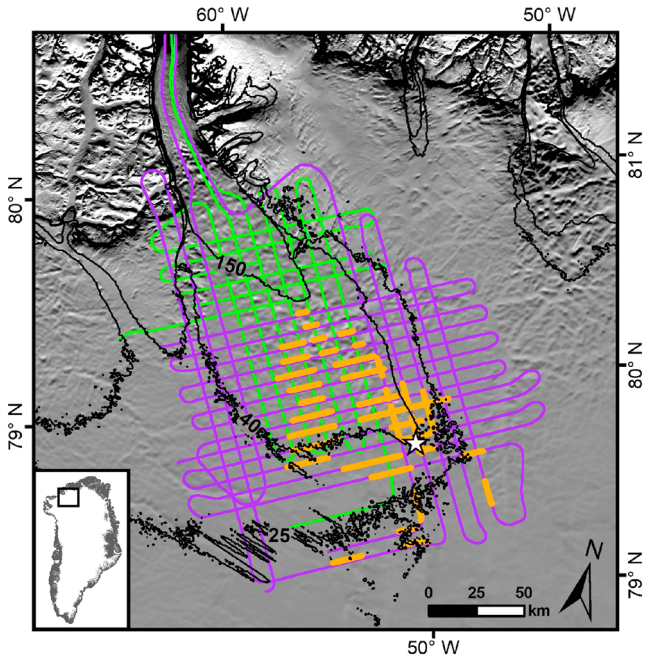

Figure 1. Study site at Petermann Glacier, Northern Greenland with National Aeronautics and Space Administration Operation IceBridge radar survey lines for 2011 P3 campaign (purple lines) and for 2010 DC-8 campaign (green lines). Background map is the Moderate-Resolution Imaging Spectroradiometer Mosaic of Greenland (Haran et al., 2013) showing the initiation of surface crevassing (star marker) that marks the "onset" of Petermann Glacier. This onset location is coincident to where Petermann Glacier begins to move faster than 40 m/year. Black lines are three selected ice velocity contours at 150, 40, and 25 m/year that highlight the major velocity transitions at Petermann (Joughin et al., 2010). Orange dots represent the locations of the deformed basal ice units mapped by Bell et al. (2014).

Petermann Glacier in Northern Greenland is an example of a broad region with high uncertainty in its basal thermal state (Figure 1). It is clear that the bed is thawed underneath the fastest flowing region (>100 m/year) near the ice sheet margin and it is frozen in the catchment interior where the ice is moving slowly (<20 m/year; MacGregor et al., 2016). The bed is also unambiguously frozen along the eastern shear margin close to an 800- to 1,300-m-deep bed canyon exists (Bamber et al., 2013). Between the well-defined thawed and frozen regions, however, there is a 50- to 150-km-wide zone where there is no agreement on the basal thermal state.

The onset of streaming for Petermann Glacier lies within this uncertain zone. Located roughly 180 km from the ice sheet margin, this onset location is marked by the initiation of surface crevassing and roughly corresponds to where the glacier begins to move faster than 40 m/year (Figure 1). In contrast to the glaciers in southeastern Greenland, Petermann Glacier is not topographically confined by a basal valley (Morlighem et al., 2014). While a 700-m-deep valley exists in the lower 80 km of the catchment, ice flow exceeding 40 m/year extends above this valley and cuts across the 100- to 150-m-high basal plateau, reaching ~180 km into the ice sheet interior (Joughin et al., 2010). The absence of a clear topographic control in the onset region suggests other mechanisms are responsible for governing the fast ice flow of Petermann Glacier.

One possible control on the onset location of Petermann Glacier is the spatial variation in resistance to basal sliding due to changes in basal hydrology. Radar observations have previously identified large-scale deformed basal ice structures across the onset region of Petermann (Bell et al., 2014; Dahl-Jensen et al., 2013). These deformed basal ice features, up to 1,100 m thick, vary in form from gentle folding to completely overturned layers. Above these deformed ice packages, the overlying Holocene ice stratigraphy (0–11.7 kyr) is usually deflected upward with massive drawdown on either side of the ice bodies.

There are multiple hypotheses for the mechanisms that form these deformed ice bodies. Some studies have suggested they may be related to changes in the basal thermal regime and its impact on basal sliding or basal freeze on (Bell et al., 2014; Wolovick et al., 2014). Others have proposed an internal ice sheet process related to either the rheological contrast between the glacial and interglacial ice properties (Dahl-Jensen et al., 2013) or the lateral convergence of ice sheet flow (Bons et al., 2016). Together, these studies point toward a complex interaction between the basal temperature, subglacial hydrology, and the internal deformation of ice in the onset regions of Petermann Glacier.

To investigate the nature of the control on the onset of Petermann Glacier, we use airborne ice-penetrating radar data collected by NASA Operation IceBridge to investigate the basal properties in that region. Specifically, we use bed reflectivity to constrain the basal thermal conditions to identify locations of thawed and frozen bed (Peters et al., 2005). Motivated by earlier studies in Greenland (Chu, Schroeder, et al., 2016; Jordan et al., 2016; MacGregor et al., 2015), we use a thermomechanical ice sheet model to correct for spatial variations in radar attenuation. We also map the thickness of Holocene-aged ice across Petermann Glacier and expand on earlier methods to produce robust bed reflectivities after correcting for both ice temperature and ice chemistry-dependent components of radar attenuation rates (MacGregor et al., 2016). Together, these bed reflectivity results allow us to examine the relationship between the basal thermal regime, subglacial hydrology, and the onset of Petermann Glacier.

2. IceBridge Radar Sounding Data

NASA's Operation IceBridge collected a dense 8–15 km spaced grid over Petermann over a 2-year period in March 2010 and in April and May 2011 (Figure 1). These radar data cover a total survey area of

Table 1
Characteristics of Airborne Ice Penetrating Radar System in 2010 and 2011

Campaign	Radar system	Bandwidth (MHz)	Transmit power (W)	Acquisition channel
2010 DC-8	MCoRDS	189.15–198.65	550	8
2011 P3	MCoRDS2	180–210	1,050	16

Note. MCoRDS = Multichannel Coherent Radar Depth Sounder.

90 km × 110 km, extending from the grounding line up to 200 km into the ice sheet interior. Both surveys use the Multichannel Coherent Radar Depth Sounder system (Byers et al., 2012). The radar system was operated at a 189- to 198-MHz center frequency on a DC-8 aircraft in 2010, while in 2011 it was operated at 180- to 210-MHz center frequency on a P-3 aircraft with a different antenna configuration to that of 2010 (Table 1).

To examine the bed properties of Petermann Glacier, we use the L1B synthetic aperture radar products from both years. These data were processed by the Center for Remote Sensing of Ice Sheets (CReSIS) at the University of Kansas and the data can be found on http://data.cresis.ku.edu. The basic CReSIS processing steps involve pulse compression with time and frequency windowing followed by motion compensation, coherent stacking, and focused synthetic radar processing. Further details about the CReSIS radar processing are given by Gogineni et al. (2001). The depth range resolution in ice after final processing is approximately 4.3 m with an along-track resolution of approximately 25 m.

3. Methods

Variation in radar bed reflectivities is a powerful indicator of the ice-bed interface properties. Relative differences in reflectivities can inform us about the presence of meltwater (Dowdeswell & Evans, 2004; Jacobel et al., 2009; Oswald & Gogineni, 2008), the basal thermal regime (MacGregor et al., 2016; Peters et al., 2005; Schroeder et al., 2016), and the roughness of the bed (Bingham & Siegert, 2009; Jordan et al., 2017; Macgregor et al., 2013; Schroeder et al., 2014). Subglacial water produces a stronger dielectric contrast with the overlying ice relative to the normal dry ice-bed interface. Therefore, a positive reflectivity anomaly above +10 dB from the catchment mean reflectivity is normally recognized as an indication of a wet bed. In contrast, a frozen bed is expected to produce a negative reflectivity anomaly that falls below −15 dB from the mean reflectivity (Peters et al., 2005). In this study, we use a +10dB threshold of relative reflectivity to identify regions of thawed bed and −15 dB for regions of frozen bed.

Before examining relative bed reflectivities, radar returns must be corrected for the characteristics of the radar system, power losses from geometric spreading, and attenuation within the overlying ice (MacGregor et al., 2012; Matsuoka, 2011). Here we detail our methodology to correct for these effects to calculate bed reflectivities for Petermann Glacier. We estimate bed reflectivity from radar bed echo power, [P], after correcting for the variations in radar system characteristics, [S], geometric spreading, [G], and englacial attenuation [L]:

$$[R] = [P] - [S] + [G] + [L] \tag{1}$$

where [] are notations expressed in decibels (Jacobel et al., 2009; MacGregor et al., 2007; Matsuoka et al., 2012). Birefringence in the ice crystal fabric could also influence bed echo power. However, for the bandwidth range of the IceBridge radar data used at Petermann Glacier (180–210 MHz), birefringence loss is relatively negligible (<2 dB) compared to the attenuation by dielectric absorption and geometric spreading (Fujita et al., 2006). Hence, following similar studies (Jacobel et al., 2009; Matsuoka et al., 2012; Schroeder et al., 2016), we assume the birefringence losses are negligible across Petermann and only correct for the other three terms in equation (1). We estimate the geometric spreading using aircraft height and ice thickness (MacGregor et al., 2007; Matsuoka et al., 2012; Wolovick et al., 2013). We next statistically level the geometric corrected power (Chu, Schroeder, et al., 2016) to estimate [S] and account for differences in radar system settings between the 2010 and 2011 setups (Figure 2). This leveling technique includes a least squares minimization that we apply at the crossovers between intersecting 2010 and 2011 tracks. At each crossover, we estimate the mean differences in bed power between the intersecting tracks within a 0.1-km radius and adjust the power of each track to minimize those differences. Leveling reduces the mean power offsets between 2010 and 2011 at crossover points from 43.7 to 0.19 dB.

Finally, we correct for englacial attenuation losses, [L], due to spatial variations in ice temperature and ice chemistry (MacGregor et al., 2007, 2015). [L] is related to the attenuation rate [N_a] as follows:

$$[L] = 2N_a H \tag{2}$$

where [H] is the ice thickness. We estimate these losses using an Arrhenius model (M07) developed by MacGregor et al. (2007). This model assumes the depth-averaged englacial attenuation rates are

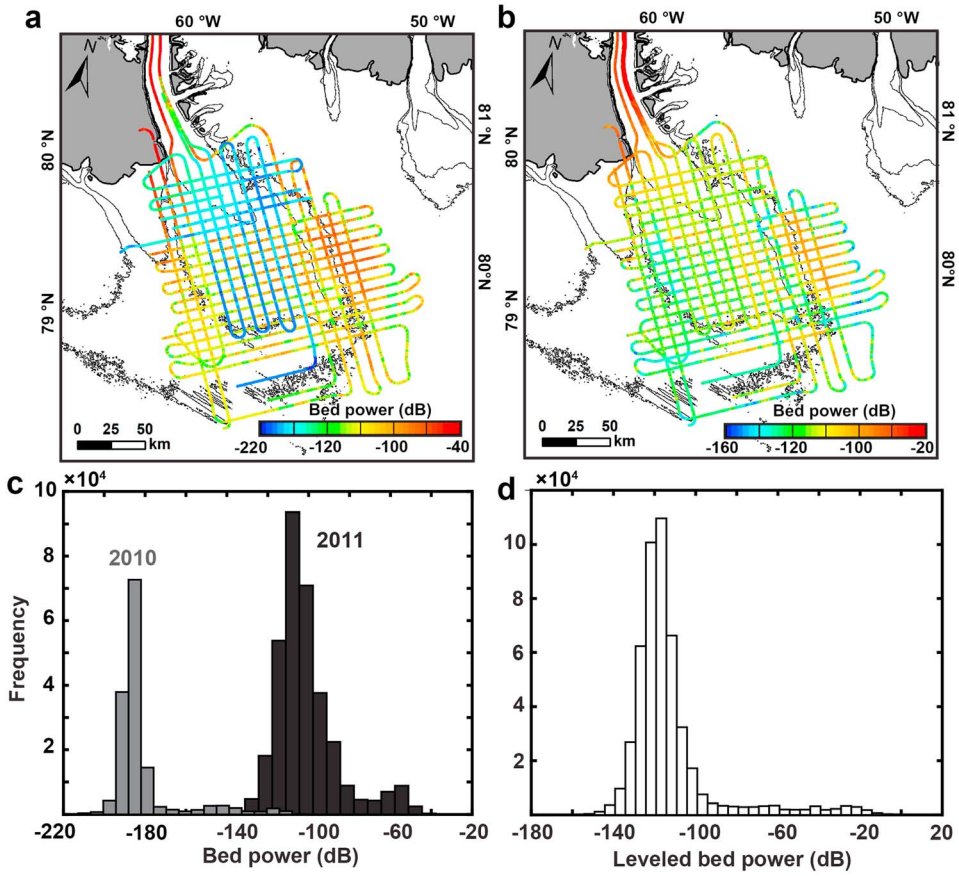

Figure 2. Geostatistical leveling to correct for differences in bed power between the 2010 and 2011 field seasons due to the changes in radar system settings. Pre-leveled bed power values shown in (a) and (c) display 80- to 100-dB offset between the two campaigns. Post-leveled values shown in (b) and (d) demonstrate a more consistent and realistic bed power distribution after leveling.

exponentially dependent on the inverse of ice temperature and linearly dependent on the chemical impurity concentration within the ice (Corr et al., 1993; MacGregor et al., 2007, 2015; Wolff et al., 1997). We first estimate ice temperature for the Petermann Glacier using a three-dimensional ice-sheet thermomechanical model, the Ice Sheet System Model (Larour et al., 2012; Morlighem et al., 2010; Seroussi et al., 2013). The model uses a full-Stokes formulation for the momentum balance with ice temperature calculated through an internal energy balance that follows an enthalpy formulation (Aschwanden et al., 2012). Ice is modeled as an incompressible material. Basal drag is estimated following a Coulomb-like sliding law (Cuffey & Paterson, 2010). We infer basal drag from satellite observations of surface velocities derived from interferometric synthetic aperture radar data using a data assimilation technique by minimizing the misfit between the modeled and observed velocities (Joughin et al., 2010). In the thermal model, a mean annual air temperature is imposed at the ice surface from Regional Atmospheric Climate Model (Noël et al., 2015). At the ice-bed interface, heat comes from both modeled geothermal heat flux (Shapiro & Ritzwoller, 2004) and the frictional heat flux estimated from the modeled basal drag. The Ice Sheet System Model's geometry is based on digital elevation models of surface topography from Howat et al. (2014) and the bed topography from Morlighem et al. (2014). A more detailed discussion of the model setup can be found in the supporting information. Next, we correct for the impact of a spatially varying ice chemistry on englacial attenuation. The amount of acid (H^+), sea-salt chloride (Cl^-), and ammonium (NH_4^+) within the ice can differ significantly across the catchment depending on the age of ice, whether it is formed in the interglacial Holocene period (0–11.7 kyr) or in the Last Glacial Period (LGP, 11.7–115 kyr; MacGregor et al., 2007). Holocene-aged ice is typically more conductive than LGP ice. For a typical temperature range of −35 to 0 °C in Greenland, Holocene-aged ice produces 3–10 dB/km higher attenuation losses than LGP ice (MacGregor et al., 2015). While the effects of spatially varying chemistry are often ignored in attenuation studies

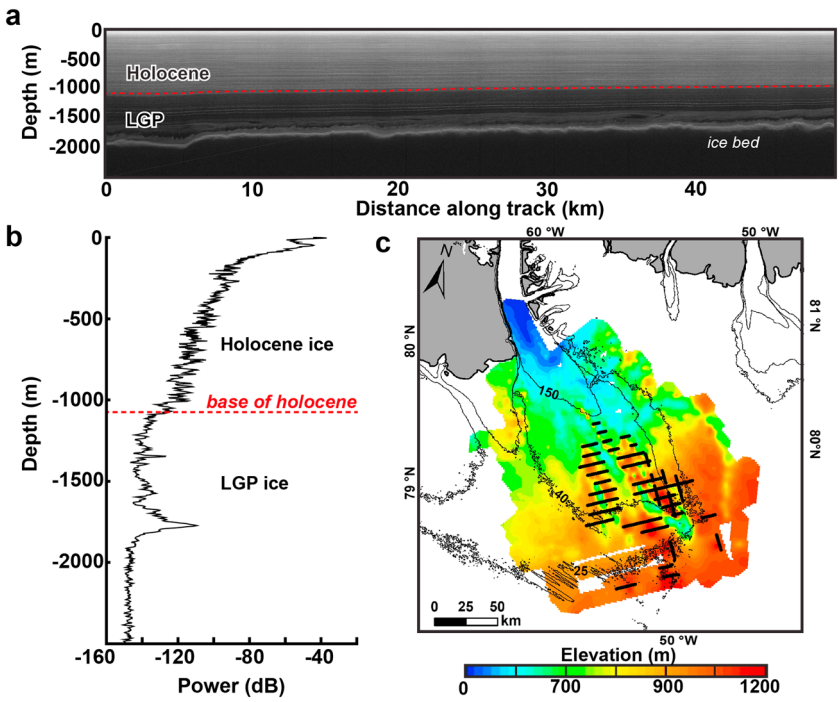

Figure 3. A map of the Holocene ice thickness across the Petermann glacier catchment. (a) Radar echogram shows a distinct stratigraphic change associated with the boundary between the brighter layered Holocene-aged ice and the dimmer Last Glacial Period (LGP) ice that was used to trace the bottom of the Holocene ice elevation (red line). (b) An example of variations in radar returned power with depths showing the base of the Holocene ice is coincident with a reduction in radar power. (c) Elevation of the base of the Holocene ice mapped across the glacier catchment.

(Jordan et al., 2016), in the case of Petermann Glacier we need to account for these effects because the presence of deformed basal ice introduces tremendous variations in the Holocene and LGP ice thickness across the region (Figure 3c; Bons et al., 2016; Dahl-Jensen et al., 2013). To correct for the spatial varying ice chemistry, we trace the base of the Holocene ice across Petermann Glacier (Figure 3). We identify this boundary by linking the radar reflections to the ice-age chronology of the nearby North Greenland Eemian Ice Drilling ice core (Rasmussen et al., 2013). Our layer tracing method follows Karlsson et al. (2013), and we use the distinct decrease in radar echo power to identify the transition from the brighter Holocene ice to the dimmer LGP ice (Figure 3b). While we can use this method to automatically trace the base of Holocene ice in the lower 100 km of Petermann Glacier, deformed ice bodies often significantly disrupted the ice stratigraphy in the ice sheet interior. Around these deformed bodies, the elevation of the Holocene-LGP transition can shift by more than 500 m. We can identify and trace these sharp changes in elevation using manual digitization. The LGP ice thickness is then given by the difference between total ice thickness and the elevation of the base of Holocene ice. Finally, both the modeled ice temperatures and the mapped Holocene and LGP ice thickness are input into the M07 Arrhenius model to estimate the spatial variations in N_a across the Petermann Glacier catchment.

4. Radar Attenuation and Uncertainties

Attenuation rates vary spatially from 10 dB/km at the eastern shear margin to more than 25 dB/km in the fast-flowing ice tongue (>100 m/year; Figure 4a). The variation in N_a far exceeds its estimated uncertainty ($\widetilde{N_a}$), even in the fast-moving region where warm and fractured ice could impact radar returns the most (Figure 4b). The uncertainty in N_a is the greatest source of error relative to the other terms in equation (1) (Matsuoka, 2011). For an uncertainty in ice thickness retrieval of 4.5 m (Shi et al., 2010), we estimate the uncertainty in [G] to be <0.5 dB. The uncertainty in [S], given by the maximum crossover error in bed power after leveling, is approximately 1.3 dB. The uncertainty for ignoring birefringence loss in an environment with a strongly developed ice crystal fabric is <2 dB given the IceBridge radar frequency is <210 MHz and the

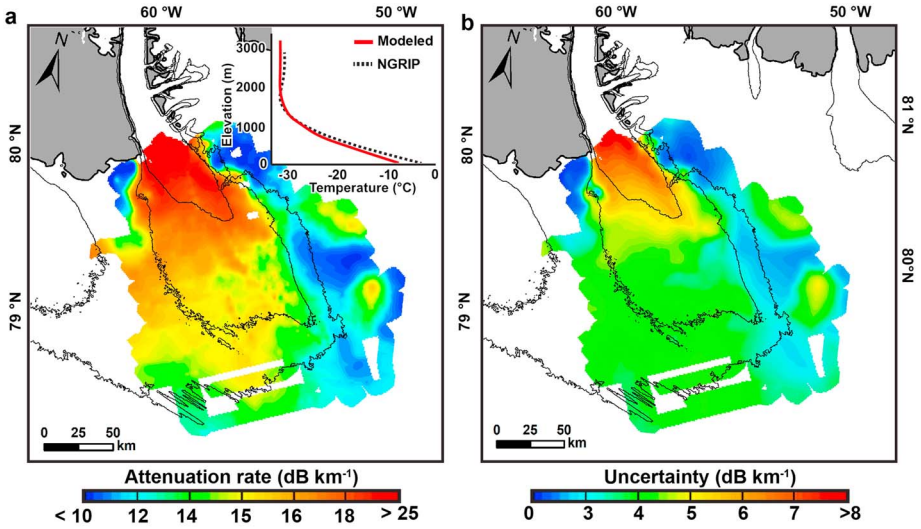

Figure 4. (a) Calculated englacial attenuation rates. (b) Total error in the attenuation rates calculated. It includes uncertainties in the modeled ice temperature and from tracing the thickness of the Holocene ice. Uncertainties in the modeled temperature are defined as the mean difference between the observed borehole temperature at the NorthGRIP ice core (Dahl-Jensen et al., 2003) and the modeled ice column temperature at the same site (see inset in a). NGRIP/NorthGRIP = North Greenland Ice Core Project.

bandwidth is wider than 10% of the center frequency (Matsuoka et al., 2009). In contrast, $\widetilde{N_a}$ can be greater than 8 dB/km, although across most of Petermann Glacier catchment $\widetilde{N_a}$ is less than 5 dB/km.

To calculate the uncertainty in N_a, we sum up the errors from the temperature and ice chemistry corrections as follows, $\widetilde{N_a} = \widetilde{N_a^T} + \widetilde{N_a^C}$, where $\widetilde{N_a^T}$ is the error in ice temperature estimates from the thermomechanical model, while $\widetilde{N_a^C}$ is the error related to the chemistry correction. We estimate $\widetilde{N_a^T}$ by comparing modeled temperatures to the closest available ice core temperature measurements from NorthGRIP (Figure 4a, inset; Dahl-Jensen et al., 2003). The mean −3.23 °C difference between our modeled depth-averaged temperatures and the ice core temperatures translates to a $\widetilde{N_a^T} = -1.93$ dB/km. Similarly, we estimate $\widetilde{N_a^C}$ associated with the ice chemistry correction. We define $\widetilde{N_a^C}$ by defining this error as the uncertainty related to the retrieval of the base of the Holocene ice, as this represents the largest uncertainty by far compared to other factors that may influence estimation of $\widetilde{N_a^C}$. Other sources of error related to the estimations of ice conductivities, molar conductivities and activation energy of major ions contribute to ~1 dB/km of uncertainties to our $\widetilde{N_a^C}$ estimates (MacGregor et al., 2015). We calculate the uncertainty related to the retrieval of the base of the Holocene ice by differencing the N_a^C estimates assuming 100% Holocene ice versus 100% LGP ice. The values of $\widetilde{N_a^C}$ range from 1 to 8 dB/km, with the largest error values are located near the coast beneath the fast-moving ice and where radar reflections are difficult to distinguish. This uncertainty is a maximum estimate and the actual value associated with identifying the base of the Holocene ice should fall between using a 100% Holocene and 100% LGP ice chemistry. Overall, $\widetilde{N_a^C}$ is smaller than the spatial variation in N_a even along the fast-moving ice near the coast.

5. Results

After correcting for the effects mentioned above, spatial variations in the resulting radar bed reflectivity represent the combined effect of changes in the basal dielectric contrast and in the bed roughness. From here forth, following earlier radar studies, we will express bed reflectivity relative to the catchment mean of the corrected dataset (e.g., Macgregor et al., 2011; Schroeder et al., 2016).

Figure 5a shows that the resulting relative bed reflectivities vary from −18 to +20 dB and reveal several regions of anomalously low and high bed reflectivities that correlate with the bed topography and the ice velocity structure of Petermann Glacier. In general, we observe higher reflectivities (>+10 dB) beneath the

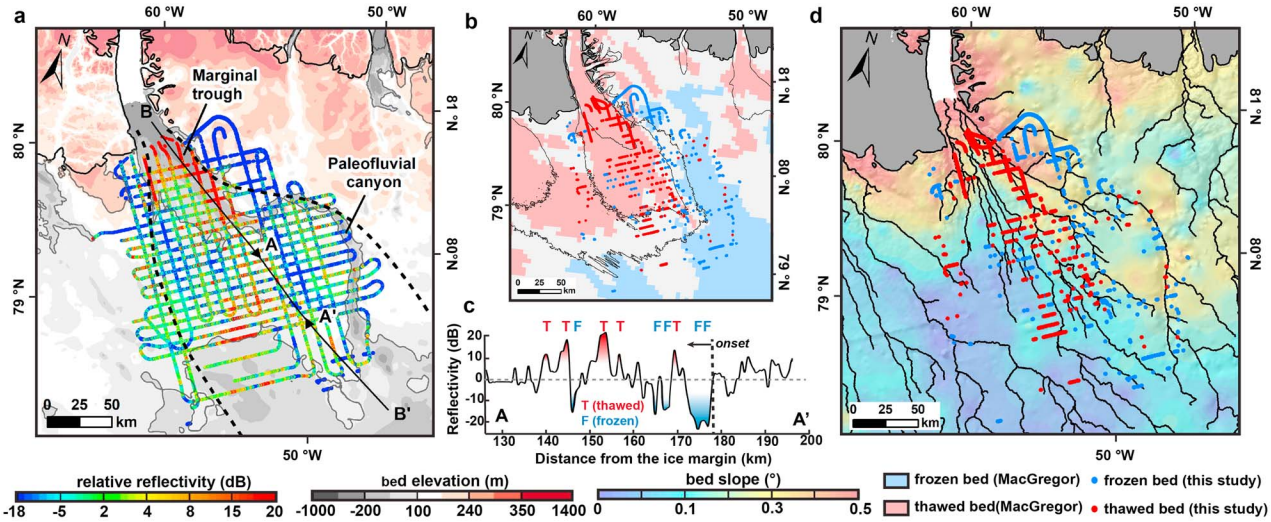

Figure 5. (a) Calculated radar bed reflectivity on top of a map of bed elevation (Morlighem et al., 2014) with a 0-m bed elevation contour (grey line). A black line indicates the location of the profile shown in Figures 5c (A-A′) and 6b (B-B′). (b) Interpretation of the basal thermal regime based on bed reflectivity (Data Sets S1 and S2). We interpret reflectivity greater +10 dB as thawed bed and reflectivity smaller than −15 dB as frozen bed. Also shown are the150-, 40-, and 25-m/year velocity contours (black lines) (Joughin et al., 2010). Background map is the basal thermal condition previously derived by MacGregor et al. (2016). (c) Bed reflectivity profile displaying multiple frozen-to-thawed thermal transitions near the onset of Petermann Glacier (>40 m/year). (d) Locations of thawed/frozen bed overlaying a bed slope map (Morlighem et al., 2014) with estimated subglacial water routing assuming that a uniform water pressure equals to ice overburden pressures (black lines) (Chu, Creyts et al., 2016).

fastest moving ice (>150 m/year) close to the coast and lower reflectivities beneath the slower moving ice sheet (Figure 5a and Figure 6b). Close to the ice sheet margin, high reflectivities are localized along the eastern side of the subglacial trough where the bed elevations are 100–500 m below sea level (labeled marginal trough in Figure 5a). In contrast, 150 km above the fast-flowing margin, the slower moving ice (<40 m/year) in the interior of Petermann Glacier is characterized by lower bed reflectivities (<−15 dB).

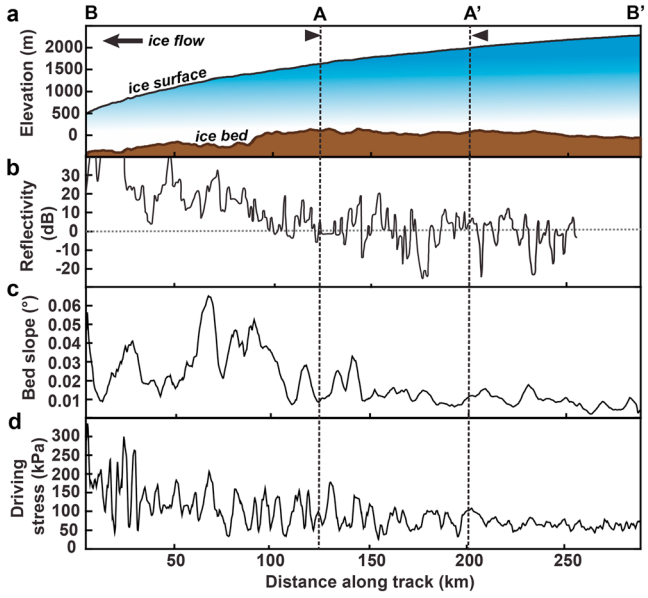

Figure 6. Ice profile extracted along a ice flow line B-B′ showing (a) ice surface and bed elevations, (b) bed reflectivity, (c) bed slope, and (d) driving stress. The dotted black lines (A-A′) highlights the region covered by the zoom-in radar bed reflectivity profile shown in Figure 5c.

A region of highly spatially variable bed reflectivities marks the transition between the fast, marginal ice and the slower moving interior ice (Figure 5c). Around the onset location (>40 m/year) where surface crevassing initiates, bed reflectivities vary from −15 to >+10 dB roughly over a 10- to 15-km length scale. Within 50 km from the onset of Petermann Glacier, we observe approximately five low reflectivity patches interspersed between five higher reflectivity patches. The higher reflectivity patches occur at increased frequency as ice velocity increases downstream from this onset region.

Outside the ice trunk of Petermann Glacier, the eastern shear margin is characterized by low bed reflectivity, while localized high reflectivity is observed along the western margin where Humboldt Glacier and Petermann Glacier converge. Along the eastern shear margin, the 1,800- to 2,400-m-deep paleofluvial canyon generally has low reflectivity less than −15 dB from the regional mean reflectivities (Figure 5a). However, isolated high-reflectivity regions can also be found along the steepest sloping (> 0.3°) stretches of the canyon (Figure 5d).

6. Discussion

6.1. Interpretation of Radar Bed Reflectivities

We interpret the pattern in Petermann catchment primarily produced by the presence of meltwater and changes in basal thermal regime.

While variations in bed roughness can also affect the spatial distribution of radar bed reflectivity (Jordan et al., 2017; Macgregor et al., 2013), roughness characterized by abruptness index of radar bed echo power indicates that most of the Petermann ice trunk has a rough interface whereas the shear margin has a smoother bed (Jordan et al., 2017). If bed roughness was the dominant pattern observed in bed reflectivity, we would expect to see higher reflectivities in the smoother shear margin and lower reflectivities in the rougher ice trunk. Instead, we observe the opposite pattern, indicating the observed variations in bed reflectivity is not primarily associated with bed roughness, and therefore more likely to reflect the presence of meltwater and shifts in the basal thermal regime from frozen to thawed bed.

Near the ice sheet margin, the presence of subglacial meltwater can explain the very high ($>$ +15 dB) reflectivities beneath the fastest-flowing section of the ice trunk ($>$ 150 m yr^{-1}). The observed reflectivity range of +15 to $>$ +20 dB lies within the expected values for water ponding at the ice-bed interface (Dowdeswell & Evans, 2004; Peters et al., 2005; Schroeder et al., 2016). Within this region, our thermal model estimates high rates of basal melting ($>$ 0.2 m yr^{-1}). Enhanced shear heating associated with sliding and thicker ice in the 700- to 800-m-deep basal valley likely generates substantial melt beneath the fast-flowing trunk. Additionally, satellite imagery shows evidence of surface melt ponds close to the grounding line that could drain to the bed and potentially contribute to the observed subglacial meltwater.

Outside of the fast-flowing ice trunk, bed reflectivities decrease significantly by 13 to 25 dB. Along the eastern shear margin, bed reflectivities can be as low as – 22 dB. The shift from high to lower bed reflectivity across the ice trunk to the shear margin is likely associated with the transition from a thawed to a frozen bed (Peters et al., 2005). As these changes in reflectivity exceed the typical 3–10 dB change expected for a shift from a wet and drained bed (Macgregor et al., 2013; Schroeder et al., 2016), changes in subglacial drainage cannot be the only cause of the observed bed reflectivity variations. It is possible the temperature of the bed and a frozen bed could produce such low reflectivity values. In these low-reflectivity regions, our thermal model yields basal temperatures of -8 to -11 °C, supporting the hypothesis of a frozen bed along the shear margin. In addition to the shear margin, we observe other low-reflectivity regions (-12 to -20 dB) along the western part of the Petermann ice trunk. Similarly, these reflectivities are much lower than those typically associated with a drained, unfrozen bed (Peters et al., 2005). Bed roughness does not vary significantly across these low-reflectivity regions (Jordan et al., 2017). Localized frozen bed conditions are therefore most likely to be the origin of these low reflectivities across the slow-moving (50–60 m/year) part of the western ice trunk.

This general pattern of a largely thawed bed beneath the ice trunk and a frozen bed along the shear margins is in good agreement with an earlier study that combines several ice-flow models and radar data inversions technique (MacGregor et al., 2016; Figure 5b). Our study resolves the variations in the basal thermal regime beneath Petermann Glacier at a higher resolution than the previous study, particularly around the onset region of fast flow where ice velocity begins to exceed 40 m/year. The onset region of fast flow is coincident with the initiation of significant surface crevasses that we observe from satellite imagery (Haran et al., 2013). To investigate the basal thermal regime at this onset region more closely, we extract a profile of radar bed reflectivity along an ice flow line (Figures 5c and 6b).

6.2. Observations of Basal Thermal Regime Across the Onset of Petermann

The profile of bed reflectivity along an ice flow line shown in Figure 5c reveals multiple sharp transitions (2–4 dB/km) between lower and higher bed reflectivities at ~10- to 20-km length scales within 50 km from the onset region. The amplitude of these reflectivity variations is large from 22 to 30 dB, and therefore, likely associated with multiple transitions between a frozen to a thawed bed across the onset region. Close to the onset of Petermann Glacier, we identify several alternating frozen-to-thawed bed transitions as the ice moves away from the onset. Above these frozen and thawed patches, driving stresses varying between 50 and 150 kPa on a similar 10- to 20-km scale (Figure 6d). The driving stress typically increases over the frozen patches and decreases over the thawed bed. While our ice sheet model does not have enough resolution to capture these changes in the form of basal stresses, an earlier inversion study reveals similar organized patterns of basal drag (Sergienko et al., 2014) that we suggest are related to the multiple thawed and frozen bed transitions present near the onset of the Petermann Glacier.

From borehole temperature, radar sounding, and modeling studies, we generally expect a rise in basal temperature with increasing distances from the ice divide as both surface temperatures and strain heating

increase towards the ice sheet margin (Aschwanden et al., 2012; Dahl-Jensen, 1989; Harrington et al., 2015; MacGregor et al., 2016). Our study shows that, while this general thermal gradient holds for the Petermann Glacier, the transition where the bed shifts from frozen to thawed conditions is not a step transition occurring at a single point. Instead, our observations show that the glacier bed shifts from mostly frozen to mostly thawed through multiple transitions (Figure 5c). Variations in ice thickness, horizontal ice flow, and vertical ice flow from the interior to the margin of the ice sheet should produce a more gradual change in the basal thermal regime, and thus, these processes are unlikely to have caused the alternating bands of frozen and thawed bed. The multiple basal thermal transitions are more likely either produced by changes in water drainage across the sides of the ice trunk or by variable local heating at the base through varying basal drag or geothermal heating.

Steady state calculations of basal water routing (Chu, Creyts, et al., 2016) indicates that water can infiltrate the ice trunk either through basal overdeepening near the ice divide or via the paleofluvial canyon along the eastern shear margin (Figure 5d). However, both of these bed features are located at 30–70 km away from the onset region where we observe the alternating frozen and thawed beds. Therefore, lateral injection of meltwater likely plays a minor role in producing local variations in the basal thermal regime across the onset of Petermann Glacier. Alternatively, variable frictional heating at the base through local varying basal drag could have produced these alternating bands of thawed and frozen beds. While geothermal heating can also produce local basal melting, no existing studies have provided any evidence of local (tens of kilometers) variations in geothermal heat fluxes across the onset of Petermann Glacier. In contrast, variations in basal shear stresses (Sergienko et al., 2014) and driving stresses (Figure 6d) suggest that basal drag and thus frictional heating vary locally across the onset of Petermann Glacier. The presence of variable basal drag also broadly agrees with earlier modeling studies in Petermann Glacier (Wolovick et al., 2014). Together, our results indicate that the onset location of Petermann Glacier is more likely to be thermally controlled by local changes in frictional heating along the ice sheet base. Given the lack of apparent topographic pinning of the onset location, the upstream margin of Petermann Glacier is likely vulnerable to migration, sensitive to both changes in advective cooling and frictional heating along the ice-sheet base.

7. Conclusions

We use radar bed reflectivity to characterize the basal thermal regime of the Petermann Glacier. Using a thermomechanical model and mapping the thickness of Holocene ice, we calculate reflectivities that are corrected for both spatial variations in ice temperature and ice chemistry. The resulting bed reflectivities reveal large changes that are primarily associated with local variations in basal freezing and melting across the Petermann Glacier. Our estimates are broadly consistent with earlier calculations but reveal a more complex, spatially variable basal thermal regime across the Petermann Glacier (MacGregor et al., 2016; Oswald & Gogineni, 2012). As the base of the ice sheet shifts from a mostly frozen to a mostly thawed state with increasing distances from the ice divide, our results suggest that this thermal transition occurs multiple times across the onset of Petermann Glacier. The alternating frozen and thawed bed conditions across the onset of Petermann Glacier suggest that competing processes between advective cooling and frictional heating strongly control the onset location of Petermann Glacier. Given surface ablation is predicted to increase in a warming climate (Hanna et al., 2008; Tedesco et al., 2015), the increased meltwater availability within the catchment may cause the fast-flow region of the Petermann Glacier to reach further inland. Current thermomechanical modeling studies often disagree on the location of ice streams and the slow-flowing glaciers in the interior of the Greenland ice sheet. We suggest that the complexity of the basal thermal regime that we have observed near these onset regions could partially explain the difficulty in constraining the upstream margins of glaciers accurately in models. Future targeted geophysical measurements at the onset of glaciers will provide useful constraints for the thermal spin-ups of ice sheet models and capture the complex flow evolution of glaciers and ice streams.

Acknowledgments

W. C. is supported by NASA cryosphere grant (NNX16AJ95G). D. M. S. and T. T. C. are supported by grants from the NASA Cryospheric Sciences Program. H. S. is supported by grants from the NASA Cryospheric Sciences and Sea Level Rise Programs. R. E. B. is supported by grants from National Science Foundation (NSF) and NASA Cryospheric Sciences. We would like to thank Elisa Mantelli for insightful discussion about the processes behind the observed bed reflectivity pattern. We acknowledge the use of CReSIS data products generated with support from the University of Kansas, NSF grant ANT-0424589, and NASA Operation IceBridge grant NNX16AH54G. Radar data are available on the CReSIS data repository at https://data. cresis.ku.edu/data/rds/. Bed topography map are available on the National Snow and Ice Data Center under IceBridge BedMachine Greenland, Version 3 (https://nsidc.org/data/idbmg4). The results on the locations of the identified frozen and thawed bed are included in the supporting information. Any additional data may be obtained from W. C. (email: wchu28@stanford.edu).

References

Aschwanden, A., Bueler, E., Khroulev, C., & Blatter, H. (2012). An enthalpy formulation for glaciers and ice sheets. *Journal of Glaciology*, *58*(209), 441–457. https://doi.org/10.3189/2012JoG11J088

Bamber, J. L., Siegert, M. J., Griggs, J. A., Marshall, S. J., & Spada, G. (2013). Paleofluvial mega-canyon beneath the central Greenland ice sheet. *Science*, *341*(6149), 997–999. https://doi.org/10.1126/science.1239794

Bell, R. E., Tinto, K., Das, I., Wolovick, M., Chu, W., Creyts, T. T., et al. (2014). Deformation, warming and softening of Greenland's ice by refreezing meltwater. *Nature Geoscience*, *7*(7), 497–502. https://doi.org/10.1038/ngeo2179

Bingham, R. G., & Siegert, M. J. (2009). Quantifying subglacial bed roughness in Antarctica: Implications for ice-sheet dynamics and history. *Quaternary Science Reviews*, *28*(3–4), 223–236. https://doi.org/10.1016/j.quascirev.2008.10.014

Bons, P. D., Jansen, D., Mundel, F., Bauer, C. C., Binder, T., Eisen, O., et al. (2016). Converging flow and anisotropy cause large-scale folding in Greenland's ice sheet. *Nature Communications*, *7*, 11,427. https://doi.org/10.1038/ncomms11427

Byers, K. J., Harish, A. R., Seguin, S. A., Leuschen, C. J., Rodriguez-Morales, F., Paden, J., et al. (2012). A modified wideband dipole antenna for an airborne VHF ice-penetrating radar. *IEEE Transactions on Instrumentation and Measurement*, *61*(5), 1435–1444. https://doi.org/10.1109/TIM.2011.2181780

Chu, W., Creyts, T. T., & Bell, R. E. (2016). Rerouting of subglacial water flow between neighboring glaciers in West Greenland. *Journal of Geophysical Research: Earth Surface*, *121*(5), 925–938. https://doi.org/10.1002/2015JF003705

Chu, W., Schroeder, D. M., Seroussi, H., Creyts, T. T., Palmer, S. J., & Bell, R. E. (2016). Extensive winter subglacial water storage beneath the Greenland Ice Sheet. *Geophysical Research Letters*, *43*, 12,484–12,492. https://doi.org/10.1002/2016GL071538

Corr, H., Moore, J. C., & Nicholls, K. W. (1993). Radar absorption due to impurities in Antarctic ice. *Geophysical Research Letters*, *20*(11), 1071–1074. https://doi.org/10.1029/93GL01395

Cuffey, K., & Paterson, W. S. (2010). *The physics of glacier* (4th ed.). Oxford, UK: Butterworth-Heinemann/Elsevier.

Dahl-Jensen, D. (1989). Steady thermomechanical flow along two-dimensional flow lines in large grounded ice sheets. *Journal of Geophysical Research*, *94*(B8), 10,355–10,362. https://doi.org/10.1029/JB094iB08p10355

Dahl-Jensen, D., Albert, M. R., Aldahan, A., Azuma, N., Balslev-Clausen, D., Baumgartner, M., et al. (2013). Eemian interglacial reconstructed from a Greenland folded ice core. *Nature*, *493*(7433), 489–494. https://doi.org/10.1038/nature11789

Dahl-Jensen, D., Gundestrup, N., Gogineni, S. P., & Miller, H. (2003). Basal melt at NorthGRIP modeled from borehole, ice-core and radio-echo sounder observations. *Annals of Glaciology*, *37*(1), 207–212. https://doi.org/10.3189/172756403781815492

Dowdeswell, J. A., & Evans, S. (2004). Investigations of the form and flow of ice sheets and glaciers using radio-echo sounding. *Reports on Progress in Physics*, *67*(10), 1821–1861. https://doi.org/10.1088/0034-4885/67/10/R03

Fujita, S., Maeno, H., & Matsuoka, K. (2006). Radio wave depolarization and scattering within ice sheets: A matrix based model to link radar and ice core measurements and its application. *Journal of Glaciology*, *52*(178), 407–424. https://doi.org/10.3189/172756506781828548

Gogineni, S., Tammana, D., Stiles, J., Allen, C., & Jezek, K. (2001). Coherent radar ice thickness measurements over the Greenland ice sheet. *Journal of Geophysical Research*, *106*(D24), 33,761–33,772.

Greve, R. (1997). Application of a polythermal three-dimensional ice sheet model to the Greenland Ice Sheet: Response to steady-state and transient climate scenarios. *Journal of Climate*, *10*(5), 901–918. https://doi.org/10.1175/1520-0442(1997)010<0901:AOAPTD>2.0.CO;2

Hanna, E., Huybrechts, P., Steffen, K., Cappelen, J., Huff, R., Shuman, C., et al. (2008). Increased runoff from melt from the Greenland Ice Sheet: A response to global warming. *Journal of Climate*, *21*(2), 331–341. https://doi.org/10.1175/2007JCLI1964.1

Haran, T., Bohlander, J., Scambos, T., Painter, T., & Fahnestock, M. (2013). MEaSUREs MODIS Mosaic of Greenland 2005 (MOG2005) Image Map, Version 1. Boulder, CO. NSIDC: National Snow and Ice Data Center.

Harrington, J. A., Humphrey, N. F., & Harper, J. T. (2015). Temperature distribution and thermal anomalies along a flowline of the Greenland ice sheet. *Annals of Glaciology*, *56*(70), 98–104. https://doi.org/10.3189/2015AoG70A945

Howat, I. M., Negrete, A., & Smith, B. E. (2014). The Greenland Ice Mapping Project (GIMP) land classification and surface elevation data sets. *The Cryosphere*, *8*(4), 1509–1518. https://doi.org/10.5194/tc-8-1509-2014

Jacobel, R. W., Welch, B. C., Osterhouse, D., Pettersson, R., & MacGregor, J. A. (2009). Spatial variation of radar-derived basal conditions on Kamb Ice Stream, West Antarctica. *Annals of Glaciology*, *50*(51), 10–16. https://doi.org/10.3189/172756409789097504

Jay-Allemand, M., Gillet-Chaulet, F., Gagliardini, O., & Nodet, M. (2011). Investigating changes in basal conditions of Variegated Glacier prior to and during its 1982-1983 surge. *The Cryosphere*, *5*(3), 659–672. https://doi.org/10.5194/tc-5-659-2011

Jordan, T. M., Bamber, J. L., Williams, C. N., Paden, J. D., Siegert, M. J., Huybrechts, P., et al. (2016). An ice-sheet-wide framework for englacial attenuation from ice-penetrating radar data. *The Cryosphere*, *10*(4), 1547–1570. https://doi.org/10.5194/tc-10-1547-2016

Jordan, T. M., Cooper, M. A., Schroeder, D. M., Williams, C. N., Paden, J. D., Siegert, M. J., & Bamber, J. L. (2017). Self-affine subglacial roughness: Consequences for radar scattering and basal water discrimination in northern Greenland. *The Cryosphere*, *11*(3), 1247–1264. https://doi.org/10.5194/tc-11-1247-2017

Joughin, I., Smith, B. E., Howat, I. M., Scambos, T., & Moon, T. (2010). Greenland flow variability from ice-sheet-wide velocity mapping. *Journal of Glaciology*, *56*(197), 415–430. https://doi.org/10.3189/002214310792447734

Karlsson, N. B., Dahl-Jensen, D., Gogineni, S. P., & Paden, J. D. (2013). Tracing the depth of the Holocene ice in North Greenland from radio-echo sounding data. *Annals of Glaciology*, *54*(64), 44–50. https://doi.org/10.3189/2013AoG64A057

Kleiner, T., Rückamp, M., Bondzio, J. H., & Humbert, A. (2015). Enthalpy benchmark experiments for numerical ice sheet models. *The Cryosphere*, *9*(1), 217–228. https://doi.org/10.5194/tc-9-217-2015

Larour, E., Seroussi, H., Morlighem, M., & Rignot, E. (2012). Continental scale, high order, high spatial resolution, ice sheet modeling using the Ice Sheet System Model (ISSM). *Journal of Geophysical Research*, *117*, F01022. https://doi.org/10.1029/2011JF002140

Macgregor, J. A., Anandakrishnan, S., Catania, G. A., & Winebrenner, D. P. (2011). The grounding zone of the Ross Ice Shelf, West Antarctica, from ice-penetrating radar. *Journal of Glaciology*, *57*(205), 917–928. https://doi.org/10.3189/002214311798043780

Macgregor, J. A., Catania, G. A., Conway, H., Schroeder, D. M., Joughin, I., Young, D. A., et al. (2013). Weak bed control of the eastern shear margin of Thwaites Glacier, West Antarctica. *Journal of Glaciology*, *59*(217), 900–912. https://doi.org/10.3189/2013JoG13J050

MacGregor, J. A., Fahnestock, M. A., Catania, G. A., Aschwanden, A., Clow, G. D., Colgan, W. T., et al. (2016). A synthesis of the basal thermal state of the Greenland Ice Sheet. *Journal of Geophysical Research: Earth Surface*, *121*, 1328–1350. https://doi.org/10.1002/2015JF003803

MacGregor, J. A., Li, J., Paden, J. D., Catania, G. A., Clow, G. D., Fahnestock, M. A., et al. (2015). Radar attenuation and temperature within the Greenland Ice Sheet. *Journal of Geophysical Research: Earth Surface*, *120*, 983–1008. https://doi.org/10.1002/2014JF003418

MacGregor, J. A., Matsuoka, K., Waddington, E. D., Winebrenner, D. P., & Pattyn, F. (2012). Spatial variation of englacial radar attenuation: Modeling approach and application to the Vostok flowline. *Journal of Geophysical Research*, *117*, F03022. https://doi.org/10.1029/2011JF002327

MacGregor, J. A., Winebrenner, D. P., Conway, H., Matsuoka, K., Mayewski, P. A., & Clow, G. D. (2007). Modeling englacial radar attenuation at Siple Dome, West Antarctica, using ice chemistry and temperature data. *Journal of Geophysical Research*, *112*, F03008. https://doi.org/10.1029/2006JF000717

Matsuoka, K. (2011). Pitfalls in radar diagnosis of ice-sheet bed conditions: Lessons from englacial attenuation models. *Geophysical Research Letters*, *38*, L05505. https://doi.org/10.1029/2010GL046205

Matsuoka, K., Pattyn, F., Callens, D., & Conway, H. (2012). Radar characterization of the basal interface across the grounding zone of an ice-rise promontory in East Antarctica. *Annals of Glaciology*, *53*(60), 29–34. https://doi.org/10.3189/2012AoG60A106

Matsuoka, K., Wilen, L., Hurley, S. P., & Raymond, C. F. (2009). Effects of birefringence within ice sheets on obliquely propagating radio waves. *IEEE Transactions on Geoscience and Remote Sensing*, *47*(5), 1429–1443. https://doi.org/10.1109/TGRS.2008.2005201

Morlighem, M., Rignot, E., Mouginot, J., Seroussi, H., & Larour, E. (2014). Deeply incised submarine glacial valleys beneath the Greenland ice sheet. *Nature Geoscience*, *7*(6), 418–422. https://doi.org/10.1038/ngeo2167

Morlighem, M., Rignot, E., Seroussi, H., Larour, E., Ben Dhia, H., & Aubry, D. (2010). Spatial patterns of basal drag inferred using control methods from a full-Stokes and simpler models for Pine Island Glacier, West Antarctica. *Geophysical Research Letters*, *37*, L14502. https://doi.org/10.1029/2010GL043853

Noël, B., van de Berg, W. J., van Meijgaard, E., Kuipers Munneke, P., van de Wal, R. S. W., & van den Broeke, M. R. (2015). Evaluation of the updated regional climate model RACMO2.3: Summer snowfall impact on the Greenland Ice Sheet. *The Cryosphere*, *9*(5), 1831–1844. https://doi.org/10.5194/tc-9-1831-2015

Oswald, G. K. A., & Gogineni, S. P. (2008). Recovery of subglacial water extent from Greenland radar survey data. *Journal of Glaciology*, *54*(184), 94–106. https://doi.org/10.3189/002214308784409107

Oswald, G. K. A., & Gogineni, S. P. (2012). Mapping basal melt under the northern Greenland ice sheet. *IEEE Transactions on Geoscience and Remote Sensing*, *50*(2), 585–592. https://doi.org/10.1109/TGRS.2011.2162072

Paterson, W. S. B. (2000). *The physics of glaciers* (3rd ed.). Oxford, UK: Pergamon.

Peters, M. E., Blankenship, D. D., & Morse, D. L. (2005). Analysis techniques for coherent airborne radar sounding: Application to West Antarctic ice streams. *Journal of Geophysical Research*, *110*, B06303. https://doi.org/10.1029/2004JB003222

Rasmussen, S. O., Abbott, P. M., Blunier, T., Bourne, A. J., Brook, E., Buchardt, S. L., et al. (2013). A first chronology for the North Greenland Eemian Ice Drilling (NEEM) ice core. *Climate of the Past*, *9*(6), 2713–2730. https://doi.org/10.5194/cp-9-2713-2013

Rogozhina, I., Petrunin, A. G., Vaughan, A. P. M., Steinberger, B., Johnson, J. V., Kaban, M. K., et al. (2016). Melting at the base of the Greenland ice sheet explained by Iceland hotspot history. *Nature Geoscience*, *9*(5), 366–369. https://doi.org/10.1038/ngeo2689

Schroeder, D. M., Blankenship, D. D., Young, D. A., Witus, A. E., & Anderson, J. B. (2014). Airborne radar sounding evidence for deformable sediments and outcropping bedrock beneath Thwaites Glacier, West Antarctica. *Geophysical Research Letters*, *41*, 7200–7208. https://doi.org/10.1002/2014GL061645

Schroeder, D. M., Grima, C., & Blankenship, D. D. (2016). Evidence for variable grounding-zone and shear-margin basal conditions across Thwaites Glacier, West Antarctica. *Geophysics*, *81*(1), WA35–WA43. https://doi.org/10.1190/geo2015-0122.1

Sergienko, O. V., Creyts, T. T., & Hindmarsh, R. C. A. (2014). Similarity of organized patterns in driving and basal stresses of Antarctic and Greenland ice sheets beneath extensive, (Figure 1). *Geophysical Research Letters*, *41*, 3925–3932. https://doi.org/10.1002/2014GL059976

Seroussi, H., Morlighem, M., Rignot, E., Khazendar, A., Larour, E., & Mouginot, J. (2013). Dependence of century-scale projections of the Greenland ice sheet on its thermal regime. *Journal of Glaciology*, *59*(218), 1024–1034. https://doi.org/10.3189/2013JoG13J054

Shapiro, N. M., & Ritzwoller, M. H. (2004). Inferring surface heat flux distributions guided by a global seismic model: Particular application to Antarctica. *Earth and Planetary Science Letters*, *223*(1–2), 213–224. https://doi.org/10.1016/j.epsl.2004.04.011

Shi, L., Allen, C. T., Ledford, J. R., Rodriguez-Morales, F., Blake, W. A., Panzer, B. G., et al. (2010). Multichannel coherent radar depth sounder for NASA Operation Ice Bridge. International Geoscience and Remote Sensing Symposium (IGARSS), 1729–1732. https://doi.org/10.1109/IGARSS.2010.5649518

Tedesco, M., Doherty, S., Fettweis, X., Alexander, P., Jeyaratnam, J., Noble, E., & Stroeve, J. (2015). The darkening of the Greenland ice sheet: Trends, drivers and projections (1981–2100). *The Cryosphere Discussions*, *9*(5), 5595–5645. https://doi.org/10.5194/tcd-9-5595-2015

Wolff, E. W., Miners, W. D., Moore, J. C., & Paren, J. G. (1997). Factors controlling the electrical conductivity of ice from the polar regions—A summary. *The Journal of Physical Chemistry B*, *101*(32), 6090–6094. https://doi.org/10.1021/jp9631543

Wolovick, M. J., Bell, R. E., Creyts, T. T., & Frearson, N. (2013). Identification and control of subglacial water networks under Dome A, Antarctica. *Journal of Geophysical Research: Earth Surface*, *118*, 140–154. https://doi.org/10.1029/2012JF002555

Wolovick, M. J., Creyts, T. T., Buck, W. R., & Bell, R. E. (2014). Traveling slippery patches produce thickness-scale folds in ice sheets. *Geophysical Research Letters*, *41*, 8895–8901. https://doi.org/10.1002/2014GL062248